GSA DATA REPOSITORY 2015174

Dating shallow thrusts with zircon (U-Th)/He thermochronometry – the shear heating connection

Matteo Maino[1], Leonardo Casini[2], Andrea Ceriani[1,3], Alessandro Decarlis[4], Andrea Di Giulio[1], Silvio Seno[1], Massimo Setti[1] and Finlay M. Stuart[5]

[1] *Dipartimento di Scienze della Terra e dell'Ambiente, Università di Pavia, via Ferrata 1, 27100 Pavia, Italy*

[2] *Università di Sassari, P.O. Box 2533, DiSBEG, via Piandanna, 4, 07100 Sassari Italy*

[3] *The Petroleum Institute, Abu Dhabi, United Arab Emirates*

[4] *IPGS/EOST, rue Blessig 1, F-67084 Strasbourg Cedex, France.*

[5] *Isotope Geosciences Unit, SUERC, Scottish Enterprise and Technology Park, Rankine Avenue, East Kilbride G75 0QF, UK*

ANALYTICAL METHODS

Zircon (U-Th)/He thermochronometry

Zircon (U-Th)/He age determinations were performed on 11 samples collected from arkosic sandstones of the Bordighera Formation and quartz- and mica-rich sandstones of Ventimiglia Flysch or Flysch Noir (Table DR3). Samples H1, H2 and H3 are from the Bordighera sandstones (hanging wall). Samples T1, T2, T3 and T4 were collected from the fault core rocks, which are constituted by a gouge of both the Bordighera sandstones and the Flysch Noir shales and sandstones. Samples D1 and D2 are from the Flysch Noir shales and sandstones constituting the footwall damage zone, while samples F1 and F2 are from the relatively

undamaged footwall rocks (Ventimiglia Flysch). Detrital zircons were separated using standard magnetic and density techniques. Inclusion-free crystals were selected on the basis of size, morphology, and color using a polarizing binocular microscope at x500 magnification. Transparent whole zircon crystals with two pyramidal terminations and undamaged surfaces were handpicked, and the crystal dimensions measured. From each sample three crystals with the same morphology and surface area-to-volume ratios were loaded into each Pt-foil capsules. The average crystal widths ranged from 39.9 to 60.2 μm, and α-recoil corrections were calculated after Hourigan et al. (2005) and Dobson et al. (2009).

(U-Th)/He age determinations were performed at the Scottish Universities Environmental Research Centre. Complete Helium extraction was achieved by heating the Pt foils using a 808 nm diode laser for 20 minutes. ^{4}He concentrations were measured by peak height comparison to a calibrated standard using a Hiden HAL3F quadrupole mass spectrometer, following the protocols of Foeken et al. (2006). All samples were reheated to ensure complete degassing. No significant (i.e. < 5%) reheat helium was observed. Two or three replicates were analyzed for each sample (Table DR1). U and Th determinations were made by isotopic dilution after Dobson et al. (2009). The degassed Pt-enclosed zircons were spiked with a known amount of ^{235}U and ^{230}Th and dissolved in a Parr™ bomb acid digestion vessel. Ion exchange column chemistry was used to remove the Pt and other matrix elements. U and Th were measured on a VG PlasmaQuad-2 ICPMS. An uncertainty of 11.9% (2σ) is assumed for individual age determination (Table DR3), based on the age reproducibility of the Fish Canyon Tuff ZHe age standard (Dobson et al., 2008). The 2σ age reproducibility of each sample was also calculated. All samples have age reproducibility comparable to the zircon age standard. In order to constrain the time-temperature (t-T) history of the fault damage zone inverse modeling of the ZHe ages

from the fault damage zone (samples T1-3; Fig. DR1) was performed using HeFTy (Ketcham, 2005).

XRD data

Fourteen samples from the fault zone and surrounding wall rocks were subjected to XRD analyses (Table DR2). Sample S6 has been collected within the gouge of the fault core. Samples S3-5 and S10-11 are from the FN shales of the footwall fault damage zone, while samples S0-2 and 1S2-13 are from the relatively undeformed footwall sandstones (Ventimiglia Flysch). Sample S7 is from the hanging wall damage zone, while samples S8-9 were collected in the undamaged hanging wall. The mineralogical composition has been determined by X-ray diffractometry (XRD) on the bulk sample (random powder) and the < 2 μm fraction (clay fraction) was separated by settling in a water column and samples were mounted as oriented aggregates on glass slides. XRD analysis were carried out using a Philips PW1800 diffractometer with CuKα radiations (50 kV, 30 mA) and a scan speed of 1°2θ/minute. The mineralogical composition of the bulk sample and oriented specimen has been estimated with routine procedures (Wilson, 1987; Moore and Reynolds, 1997) under natural conditions (air-drying) and after solvation in atmosphere of ethylene–glycol at 60°C for 6 hours. Illite crystallinity (Ic) is the measure of the Kubler index (KI), which is the equivalent of FWHM (Full Width at Half Maximum) of the 10Å illite peak on oriented samples ethylene-glycol solvated. The results of mineralogical analyses are reported in Table DR2.

Fluid inclusion data

The microthermometric measurements were performed using a Linkam THMSG 600 heating-freezing stage, calibrated with synthetic pure water and CO_2 inclusions. For calibration, we used synthetic pure H_2O (final ice melting temperature: 0.0°C, homogenization temperature:

374.1°C) fluid inclusions from SYNFLINC. Inclusions were cooled to -80°C then heated to -10°C at 50°C/min, and 0.5°C/min close to the final ice melting temperature. Total homogenization temperatures were measured by heating the fluid inclusions at a rate of 100°C/minute to 100°C, and then at 1°C/min close to the homogenization temperature. The precision is a 1.0°C for homogenization temperatures.

Homogenization temperatures were determined on 20 inclusions from a sigmoidal calcite vein included into the fault damage zone, close to the fault core (Fi1) and on 34 fluid inclusions from two calcite veins in the hanging wall (Fi2) (Table DR3). Both homogenization temperature (Th) and final ice-melting temperatures (Tm_{ice}) were measured by cycling (Goldstein and Reynolds, 1994). Salinity data are not considered here. Emphasis was placed on identifying fluid inclusion assemblages (FiA), that is, the most finely discriminated groups of petrographically associated fluid inclusions, which represent the inclusions trapped at about the same time (Goldstein and Reynolds, 1994). The data are from primary (the only inclusions displaying a clear relationship to mineral growth) and secondary fluid inclusions (aligned along trails cutting mineral growths). Liquid to vapor ratio of the primary inclusions are somewhat consistent (vapor phase representing the 20% of the total inclusion volume), indicative of the absence of major re-equilibrium. Results of the measurements from sample Fi1 and Fi2 (Fig. DR2) are shown divided into primary and secondary fluid inclusions.

THERMAL MODELING

Mathematical background

The transient advection-diffusion equation is formulated in 1D as:

$$\rho C_p \left(\frac{\partial T}{\partial t} + v_z \frac{\partial T}{\partial z}\right) = \frac{\partial}{\partial z}\left(k \frac{\partial T}{\partial z}\right) \quad (1)$$

where T is temperature (K), H is the bulk heat production rate (W/m^3), ρ is density (Kg/m^3), v_z is velocity in z direction and k is temperature-dependent thermal conductivity (Vosteen and Schellschmidt, 2003; Whittington et al., 2009). The heat equation is implemented by a finite-differences code modified from Casini (2012) and Casini et al. (2013). The bulk heat production rate term in the right-hand part of the heat equation is calculated as $H = H_s + H_r$, where H_r represent a radiogenic source and H_s is the shear heating component calculated from Turcotte and Schubert (2002):

$$H_s = \sigma_y \dot{\varepsilon} \quad (2)$$

where σy is yield stress (Pa) and $\dot{\boldsymbol{\varepsilon}}$ is the strain rate (s^{-1}) accommodated within the fault plane during slip (McKenzie and Brune, 1972; Fleitout and Froideveaux, 1980). For simplicity, we neglect the thermal effect of seismic brittle processes involving pseudotachylite development and rock pulverization (Ben Zion et al., 2012). In other words, H_s accounts only for the long-term frictional or frictional-viscous component of the strain energy dissipated along the fault. Therefore, our model provides a minimum estimate of shear heating. The mean strain rate accommodated by the thrust is calculated from the horizontal displacement accommodated by the thrust during a given time as:

$$\dot{\varepsilon} = \Delta L * tan\beta / w * \Delta t \quad (3)$$

where ΔL is the finite horizontal displacement (m), β is the fault slope angle, w is the fault zone width (m), and Δt is time (s). In the experiments, ΔL values change between 5 and 50 km. This corresponds to average strain rates between 10^{-15} and 10^{-13} s^{-1} for a fault damage zone width of 80 – 100 m, which is consistent with the geologic observations.

Deformation is simulated assuming temperature-dependent rheology. The behavior of fault rocks is assumed to be purely frictional for temperature below 200°C. In one dimension, the

yield stress corresponds to the frictional strength and it is thus calculated from the Navier-Coulomb criterion using an apparent coefficient of friction of 0.4 (Crawford et al., 2008; Bos and Spiers, 2002). At temperature above 200°C, pressure-solution become effective (Shimizu, 1995; Casini & Funedda, 2014) and stress is calculated using the frictional-viscous flow law for phyllosilicate-rich fault rocks (Bos and Spiers, 2002). Under these assumptions, the peak stress recorded in the experiments varies between about 50 and 150 MPa.

Experiment design and model set up

The model consists of 200 irregularly spaced points, half of which form a low-resolution Eulerian grid that provides constraints on the thermal structure of the Alpine crust during thrust motion. Dirichlet boundary conditions are imposed at both ends of the low-resolution profile, such as 0°C at the surface, and 1350°C at the base of a 200 km-thick the lithosphere, respectively. Compositional parameters of the model lithosphere, such as the ^{235,238}U, ^{232}Th, and ^{40}K contents, and nominal rock densities (Table DR4), were selected on the basis of published datasets (Turcotte & Schubert, 2002). The crust is divided into three layers (Table DR4), whose thickness and radiogenic heat production rate have been constrained by combining geophysical information (Grad et al., 2009), geochemistry and P-T-t paths (Brower et al., 2004; Gasco et al., 2014). Petrology and geochronological constraints indicate that the Alpine lithosphere reached a maximum thickness of 70–75 km in the early Miocene, followed by rapid uplift and exhumation (Gasco et al., 2014). Therefore, a reference bulk crustal thickness of 70 km is assumed at the beginning of the experiments, while the final Moho depth is set to 50 km (Table DR4) according to the present-day value inferred from geophysical models (Grad et al., 2002). All experiments, including those for variable displacement rates and variable duration of shear (Table DR5), start at 50 Ma, well before the beginning of thrusting, to minimize the numerical artifacts related to

the choice of initial conditions. The remaining nodes form a high-resolution grid centered on the fault core. The temperature, density, and the other physical parameters of nodes in the high-resolution domain are interpolated at each time step from the low-resolution model. The bulk heat production rate is updated by computing the H_s component from Eq. (2). Then, the coupled diffusion-advection equation (Eq. 1) is solved within the high-resolution domain on a mixed Eulerian-Lagrangian grid. The advection term is computed using a marker-based scheme (i.e., Gerya and Yuen, 2003) with one million of Lagrangian markers that portray fine details of the thermal structure around the fault zone. Finally, temperature is interpolated back from Lagrangian markers to Eulerian points. Marker-based advection is also used to simulate the circulation of hot fluids (Table DR6). The volume of fluids advected in the fault zone is expressed as $\phi = L_{hr}/L_v$, where L_{hr} and L_v are the thickness-equivalent volume of host rock and syn-tectonic veins, respectively. In the experiments, ϕ spans between 0.1 and 0.6, although typical values observed in the study area are in the range 0.1–0.2. The flow of fluids is either instantaneous or distributed. In the first case, the fault zone is injected instantaneously by a volume of fluids $V_f = \phi * w$, which maximizes heating. Otherwise the fault zone is progressively injected with a characteristic flow rate, $\dot{\varphi}_f$, given by:

$$\dot{\varphi}_f = \frac{\partial \phi}{\partial t} \quad (4)$$

In our model, fluids are sourced from the brittle-ductile transition zone corresponding to the 300°C isotherm and transported to the fault zone with an infinite velocity. In other words, fluids do not exchange temperature with the nodes outside the fault zone. Therefore, our experiments should provide a maximum estimate for the thermal effect due to circulation of hot fluids.

REFERENCES CITED

Ben-Zion, Y. and C. G., Sammis, 2013, Shear heating during distributed fracturing and pulverization of rocks: Geology, v. 41, p. 139–142, doi:10.1130/G33665.1.

Brower, F.M., van de Zedde, D.M.A., Wortel, M.J.R. and Vissers, R.L.M., 2004, Late-orogenic heating during exhumation: Alpine PTt trajectories and thermomechanical models: Earth and Planetary Science Letters, v. 220, p. 185-199. Doi: 10.1016/S0012-821X(04)00050-0

Bos, B. and Spiers, C.J., 2002, Frictional-viscous flow of phyllosilicate-bearing fault rock: Microphysical model and implications for crustal strength profiles: Journal of Geophysical Research, v. 107, B2, 2028, doi:10.1029/2001JB000301.

Byerlee, J. D., 1978, Friction of Rocks: Pure and Applied Geophysics, v. 116 (4-5), p. 615–626, doi:10.1007/BF00876528.

Casini, L., 2012, A Matlab-derived software (geothermMOD1.2) for one-dimensional thermal modeling and its application to the Corsica-Sardinia batholith, Computers & Geosciences, v. 45, p. 82-86, doi: 10.1016/j.cageo.2011.10.020.

Casini, L., and Funedda, A., 2014, Potential of pressure solution for strain localization in the baccu Locci Shear Zone (Sardinia, Italy): Journal of Structural Geology, v. 66, p. 188-204, doi: 10.1016/j.jsg.2014.05.016

Casini, L., Puccini, A., Cuccuru, S., Maino, M. and Oggiano, G., 2013, GEOTHERM: A finite difference code for testing metamorphic P–T–t paths and tectonic models: Computers & Geosciences, v. 59, p. 171-180.

Crawford, B.R., Faulkner, D.R., and Rutter, E.H., 2008, Strength, porosity, and permeability development during hydrostatic and shear loading of synthetic quartz-clay fault

gouge: Journal of Geophysical Research: Solid Earth, v. 113, B03207, doi: 10.1029/2006JB004634.

Dobson, K. J., Stuart, F. M., Dempster, T. J. and EIMF, 2008, U and Th zonation in Fish Canyon Tuff zircons: Implications for a zircon (U-Th)/He standard: Geochimica Cosmochimica Acta, v. 72, p. 4745-4755.

Dobson, K. J., Persano, C. and Stuart, F. M., 2009, Quantitative constraints on mid- to shallow crustal processes using the zircon (U-Th)/He thermochronometer, *in*: Lisker, F., Ventura, B. and Glasmacher, U. A., eds, Thermochronological methods: from palaeotemperature constraints to landscape evolution models: Geological Society London, Special Publication, v. 324, p.47-56.

Fleitout, L. and Froidevaux, C., 1980, Thermal and mechanical evolution of shear zones: Journal of Structural Geology, v. 2, p. 159-164.

Foeken, J. P. T., Stuart, F. M., Dobson, K. J., Persano, C. and Vilbert, D., 2006, A diode laser systemfor heating minerals for (U-Th)/He chronometry: Geochemistry Geophysics Geosystems, v.7, Q04015, doi:10.1029/2005GC001190.

Gasco, I., Gattiglio, M. and Borghi, A., 2014, Review of metamorphic and kinematic data from Internal Crystalline Massifs (Western Alps): PTt paths and exhumation history: Journal of Geodynamics, v. 63, p. 1-19, doi: 10.1016/j.jog.2012.09.006.

Gerya, T.V., and Yuen, D.A., 2003, Characteristics-based marker-in-cell method with conservative finite-differences schemes for modeling geological flows with strongly variable transport properties: Physics of the Earth and Planetary Interiors, v. 140, p. 293–318, doi:10.1016/j.pepi.2003.09.006.

Gleason, G.C. and Tullis, J., 1995, A flow law for dislocation creep of quartz aggregates determined with the molten salt cell: Tectonophysics, v. 247, p. 1-23, doi:10.1016/0040-1951(95)00011-B.

Goldstein, R.H. and Reynolds, T.J., 1994, Systematics of fluid inclusions in diagenetic minerals: Society for Sedimentary Geology Short Course 31: SEPM, Tulsa, OK, 199 p.

Grad, M., Brückl, E., Majdański, M., Behm, M., Guterch, A., and CELEBRATION 2000 and ALP 2002 Working Groups, 2009, The Moho depth map of the European Plate: Geophysical Journal International, v. 176, p. 279-292.

Hourigan, J. K., Reiners, P. W. and Brandon M. T., 2005, U-Th zonation-dependent alpha ejection in (U-Th)/He chronometry: Geochimica Cosmochimica Acta, v. 69, no. 13, p. 3349-3365.

Johannes, W. and Holtz, F., 1996, Petrogenesis and experimental petrology of granitic rocks: Minerals and rocks, Berlin, p.335

Ketcham, R. A., 2005, Forward and inverse modeling of low-temperature thermochronometry data, *in*: P. W., Reiners, T. A., Ehlers, eds., Low-Temperature Thermochronology: Techniques, Interpretations and Application: Review of Mineralogy and Geochemistry, v. 58, p. 275-314.

McKenzie D. and Brune J.N., 1972, Melting on Fault Planes During Large Earthquakes: Geophysical Journal of the Royal Astronomical Society, v. 29, p. 65-78.

Moore, D.M., Reynolds, R.C., 1997, X-ray Diffraction and the Identification and Analysis of Clay Minerals, 2nd ed: Oxford University Press, New York, NY, 378 p.

Patino Douce, A.E., 2004, Vapor-Absent Melting of Tonalite at 15-32 kbar: Journal of Petrology, v. 46, p. 275-290.

Petford, N., Cruden, A.R., McCaffrey, K.J.W. and Vigneresse, J.L., 2000, Granite magma formation, transport and emplacement in the Earth's crust: Nature v. 408, p. 669-673.

Platt, J. P., and Behr, W. M., 2011, Lithospheric shear zones as constant stress experiments: Geology, v. 39, p. 127-130.

Ranalli, G., 1995, Rheology of the Earth: 2nd ed. Chapman & Hall, London, 413 p.

Turcotte, D.L. and Schubert, G., 2002, Geodynamics: Cambridge University Press, Cambridge, UK, p. 472.

Vogt, K., Gerya, T.V. and Castro, A., 2012, Crustal growth at active continental margins: Numerical modeling: Physics of the Earth and Planetary Interiors, v. 192-193, p. 1-20.

Vosteen, H-D. and Schellschmidt, R., 2003, Influence of temperature on thermal conductivity, thermal capacity and thermal diffusivity for different types of rock: Physics and Chemistry of the Earth, Parts A/B/C 28, p. 499-509.

Whittington, A.G., Hofmeister, A.M. and Nabelek, P.I., 2009, Temperature-dependent thermal diffusivity of the Earth’s crust and implications for magmatism: Nature, v. 458, p. 319-321.

Wilson, M.J., editor, 1987, Handbook of Determinative Methods in Clay Mineralogy: Blackie, New York, NY, 308 p.

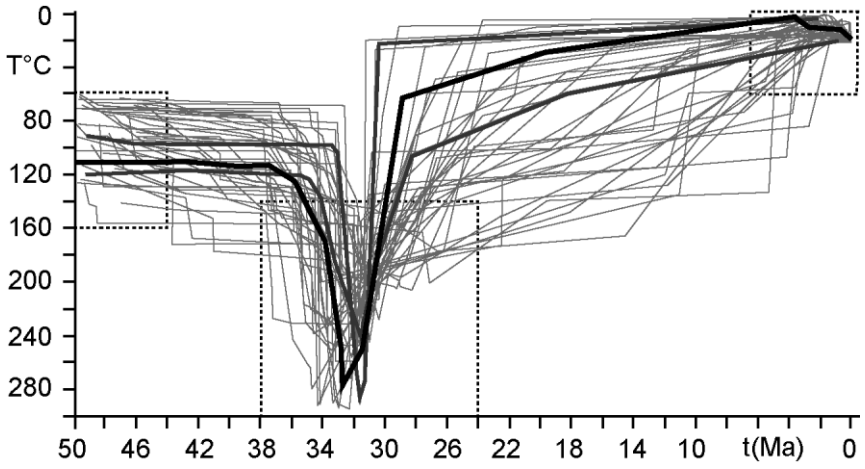

Figure DR1. Inverse modeling of ZHe data from the fault core (T1-4) using HeFTy (Ketcham, 2005). Light and dark grey lines indicate the acceptable (>50%) and good (>95%) confidence intervals respectively. The black thick line is the best fit.

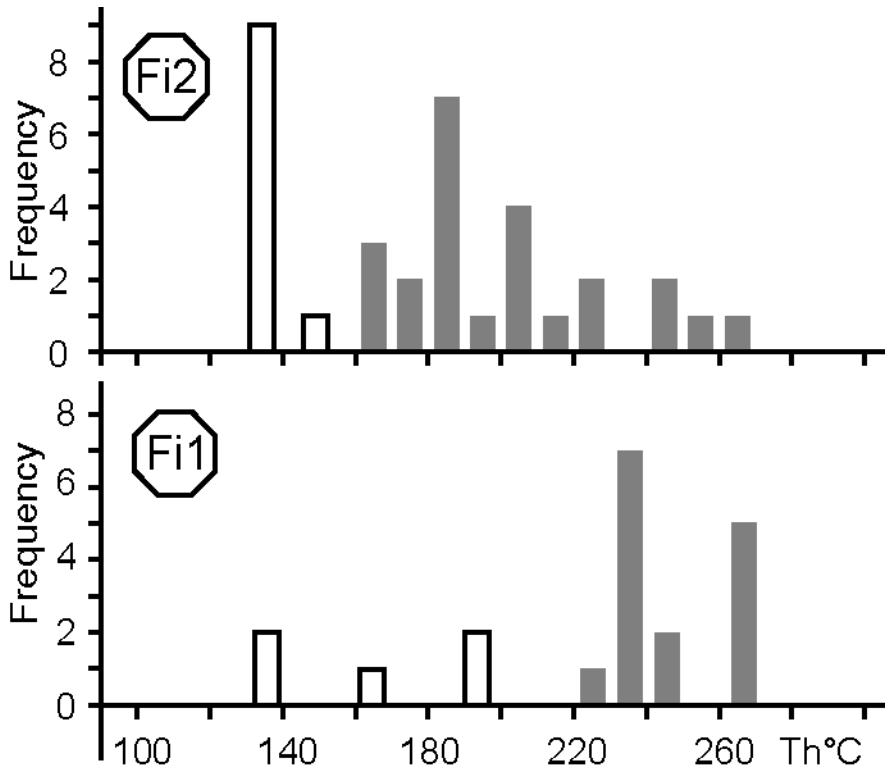

Figure DR2. Frequency plot of homogenization temperature of bi-phase aqueous fluid inclusions in calcite crystals forming syn-kinematic veins collected close to the fault core (Fi1) and in the hanging wall (Fi2). Grey bars indicate the primary fluid inclusions, while white bars are the secondary fluid inclusions.

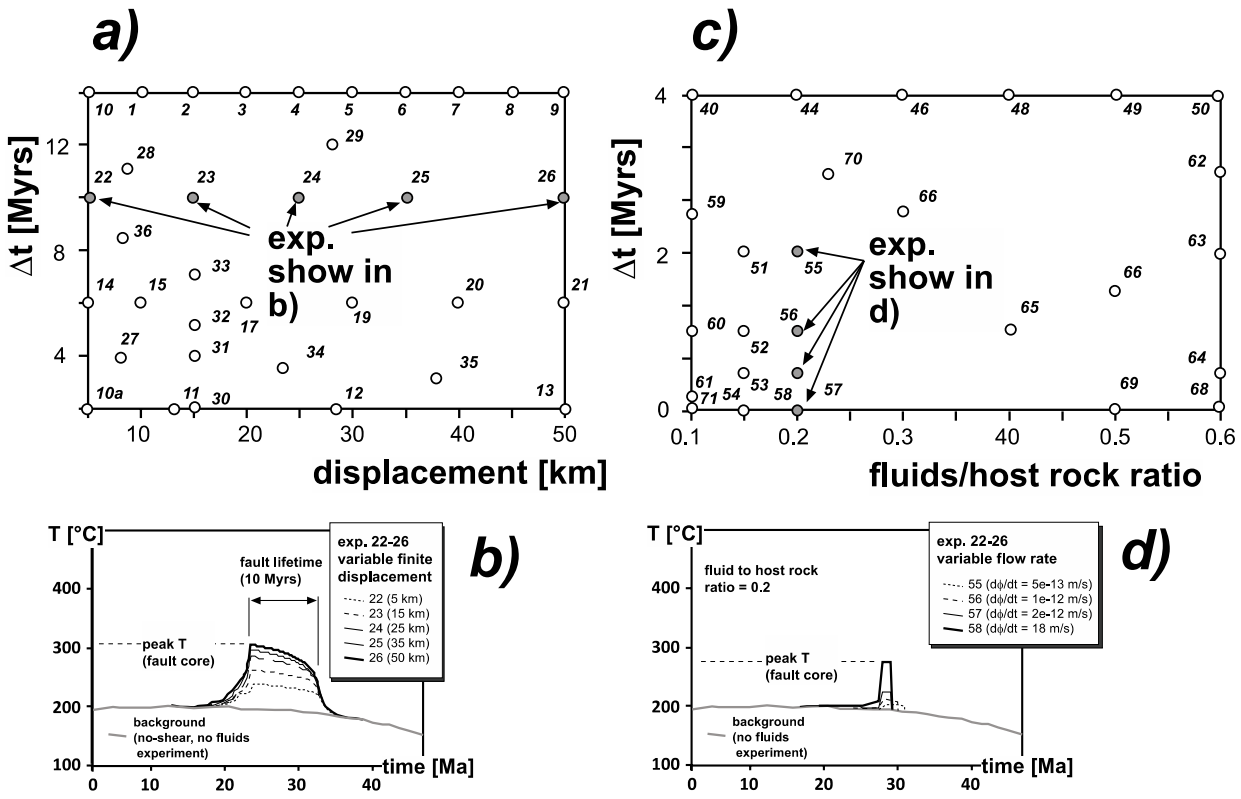

Figure DR3. Results of numerical experiments: a) summary of boundary conditions for all the shear-heating experiments (x-axis = finite displacement accommodated by the thrust [km], y-axis = duration of deformation [Myrs]); gray dots indicate the experiments shown in fig. DR1b; b) evolution of temperature in the fault core for variable finite displacement, corresponding to variable strain-rate and shear heating (experiments 22-26; Table DR5), c) summary of boundary conditions for the experiments with fluids (x-axis = volume of fluids to host-rock ratio [dimensionless], y-axis = duration of fluid flow [Myrs]; Table DR6); gray dots indicate the experiments shown in fig. DR1d; d) evolution of temperature in the fault core for variable flow rate and fluid to host-rock ratio of 0.2.

TABLE DR1
. ZIRCON (U-TH)/HE DATA

Sample /Aliquot	Sample location with respect to the fault zone	Location		Mean grain radius (μm)†	U (ng)§	Th (ng)§	4He (ncc)	Analytical error %	Raw age (Ma)	Th/U	F_T#	Corrected age (Ma)**
		Lat.	Lat.									
H1/1	Hangingwall damage zone (2m above the fault core)	4877604	399839	55.2	8.44	0.27	93.8	5.45	90.0	0.03	0.78	115.3
H1/2				45.1	13.14	4.44	151.6	3.82	87.2	0.34	0.73	119.5
										Mean ZHe Age		**117.4 ± 14**
H2/1	Hangingwall (5m above the fault core)	4877609	399843	53.9	2.30	1.45	31.4	3.92	97.0	0.63	0.77	126.0
H2/2				48.6	1.17	0.26	13.2	5.81	87.5	0.22	0.75	116.7
H2/3				39.9	1.95	1.28	25.7	3.96	93.3	0.66	0.70	133.3
										Mean ZHe Age		**125.3 ± 14.9**
H3/1	Hangingwall (25m above the fault core)	4877624	399850	51.0	7.80	1.72	123.1	3.83	122.2	0.22	0.76	160.8
H3/2				42.5	3.71	0.44	52.8	4.50	112.8	0.12	0.72	156.7
										Mean ZHe Age		**158.7 ± 18.9**
T1/1	Fault core	4877603	399820	57.0	3.70	2.16	13.2	3.84	25.7	0.59	0.78	32.9
T1/2				51.7	4.29	2.07	13.2	3.89	22.6	0.48	0.76	29.8
										Mean ZHe Age		**31.4 ± 3.7**
T2/1	Fault core	4877601	399832	56.6	4.04	1.44	14.0	3.75	26.3	0.36	0.78	33.7
T2/2				48.3	2.47	0.20	7.8	6.70	25.5	0.08	0.75	34.0
										Mean ZHe Age		**33.8 ± 4.0**
T3/1	Fault core	4877603	399837	57.5	0.70	0.32	2.0	6.30	21.3	0.46	0.78	27.5
T3/2				44.4	0.65	0.51	2.0	5.49	21.6	0.78	0.72	30.0
										Mean ZHe Age		**28.8 ± 3.4**
T4/1	Fault core	4877874	398815	59,7	108.78	34.46	384.0	1.16	26.9	0.52	0.80	33.7
T4/2				46,9	7.16	7.07	220.1	1.19	20.5	0.73	0.74	27.7
										Mean ZHe Age		**30.7 ± 3.6**
D1/1	Footwall damage zone (20m below the fault core)	4877597	399814	60.2	28.96	8.44	363.0	1.16	95.6	0.29	0.80	119.5
D1/2				52.3	33.50	10.55	395.2	2.08	89.6	0.31	0.76	117.9
										Mean ZHe Age		**118.7 ± 14.1**
D2/1	Footwall damage zone (bottom)	4877297	399521	42.1	18.97	3.83	167.1	1.19	68.5	0.20	0.72	95.2
D2/2				55.7	21.13	9.31	204.3	2.17	71.7	0.44	0.78	91.9
										Mean ZHe Age		**93.5 ± 11.1**
F1/1	Footwall (2m below the fault damage	4877290	399524	53.9	10.89	3.99	349.3	4.20	237.7	0.37	0.78	304.7

F1/2	zone)			58.8	4.84	2.51	173.1	2.48	255.9	0.52	0.80	319.9
										Mean ZHe Age		**312.3 ± 37.2**
F2/1	Footwall (25m below the fault damage zone)	4877287	399537	47.2	10.91	6.75	358.0	2.16	230.8	0.62	0.74	311,9
F2/2				44.6	4.61	2.53	141.2	3.48	218.7	0.55	0.72	303,8
										Mean ZHe Age		**307.8± 36.6**
FCT*/1				58.1	0.68	0.54	2.0	7.46	20.5	0.79	0.78	26.2
FCT*/2				47.9	0.76	0.46	1.99	5.75	18.8	0.60	0.74	25.4
FCT*/3	-	-	-	41,5	2.11	1.28	5.19	1.61	17.6	0.61	0.72	24,5
FCT*/4				60,9	2.33	1.65	7.34	1.50	22.2	0.71	0.80	27,7
										Mean ZHe Age		**26.0 ± 3.1**

All samples were collected at altitude comprised between 1450m and 1575 m, with the exception of T4, which comes from 1650 m. *FCT: Fish Canyon Tuff standard. [†] Mass Weighted Average Radius (MWAR). Multiple crystal aliquots were used for all samples, with three crystals in each sample. [§] U and Th data are corrected for a procedural blank of 0.1067 ng U and 0.0997 ng Th. Blank uncertainty is ± 10% and is included in the analytical uncertainty. [#] Recoil correction, F_T, calculated using the calculations of Hourigan et al. (2005) assuming homogeneity. ** Age uncertainties from each individual age measurement are 11.9% (calculated from the 2σ age reproducibility of the FCT age standard). For samples that show a single age population, the mean sample specific ZHe ages are shown at ± 2σ.

TABLE DR2. MINERALOGICAL COMPOSITION (%) OF THE BULK AND THE CLAY FRACTION (<2m)

Sample	Formation*/ Lithology	Structural position	Location		Bulk†								<2 µm			
			Lat.	Long.	Ch	M	Qz	K-F	Pl	Cc	Do	He	Sm	I	Ch	FWHM§ (Δ2θ CuKα)
S0	VF/shale	Footwall	4877611	399025	17	34	42	0	0	7	0	0	0	91	9	0.38
S1	VF/ shale	Footwall	4877260	399458	0	5	13	3	0	76	3	0	4	92	4	0.33
S2	VF/ shale	Footwall	4877281	399491	10	35	24	4	7	20	0	0	0	86	14	0.38
S12	VF/ shale	Footwall	4877293	399516	15	14	14	1	4	52	0	0	0	78	22	0.33
S13	VF/ shale	Footwall	4877287	399539	26	20	33	0	2	16	14	11	0	89	11	0.45
S11	FN/shale	Fault damage zone	4877296	399516	25	23	29	5	15	3	0	0	0	82	18	0.26
S10	FN/shale	Fault damage zone	4877308	399516	4	20	33	0	2	16	14	11	5	88	7	0.31
S3	FN/marl	Fault damage zone	4877594	399798	20	20	19	3	11	27	0	0	0	76	24	0.26
S4	FN/marl	Fault damage zone	4877600	399810	33	23	22	0	15	7	0	0	0	75	25	0.29
S5	FN/shale	Fault damage zone	4877603	399813	0	94	2	0	4	0	0	0	0	94	6	0.29
S6	Bor-FN/gouge	Fault core	4877607	399841	10	27	16	0	7	40	0	0	0	90	10	0.26
S7	Bor/sandstone	Hangingwall	399844	399844	17	20	12	1	3	47	0	0	0	81	19	0.31
S8	Bor/sandstone	Hangingwall	4877624	399845	13	50	19	4	6	8	0	0	0	93	7	0.36
S9	SRem/marl	Hangingwall	4877621	401816	26	59	15	0	0	0	0	0	0	84	16	0.45

* Lithostratigraphic formation. VF: Ventimiglia Flysch; FN: Flysch Noir; Bor: Bordighera sandstone; SRem: San Remo Flysch. † Whole-rock composition. Ch: chlorite; Sm: smectite; M: mica; I: illite; Qz: quartz, K-F: K-feldspars; Pl: plagioclase; Cc: calcite; Do: dolomite; He: hematite. § FWHM: Full Width at Half Maximum (10Å illite peak).

TABLE DR3 – MICROTHERMOMETRIC DATA FROM VEIN-FILLING CALCITE

Sample / Lithology / Location	FiA*	Fi†	Homogenization Temperature (Th °C)	SALINITY
Fi1	1	1	137.3	-
Flysch Noir		2	139.5	-
Lat. 4877601	2	3	165.5	-
Long. 399818		4	190.3	1.4
		5	193.4	-
	3	6	220.0	-
		7	231.2	-
		8	231.3	-
		9	234.5	-
	4	10	235.6	1.9
		11	236.7	-
		12	238.5	-
	5	13	238.8	-
		14	242.2	-
		15	248.8	-
		16	261.1	4.3
		17	262.2	3.1
	6	18	262.1	-
		19	266.5	4.2
		20	268.6	-
Fi2	1	1	130.7	-
Bordighera sandstones		2	131.8	2.6
		3	132.6	2.6
Lat. 4877623		4	133	2.6
Long. 399847		5	134.2	-
		6	135.1	2.6
	2	7	135.5	2.6
		8	136.2	3.1
		9	136.2	3.4
		10	149.5	0.7
		11	163.4	2.6
	3	12	163.4	-
		13	163.4	-
		14	173.4	-
	4	15	174.5	-
		16	180.2	-
		17	180.7	0.5
		18	181.3	-

	19	183.4	3.2
	20	185.1	-
5	21	185.6	-
	22	187.7	-
	23	195.7	-
	24	200.3	-
	25	200.8	3.7
	26	205.5	-
	27	207.9	4.0
6	28	215.5	-
	29	222.2	-
	30	224.7	3.5
	31	241.0	-
	32	241.2	-
	33	251	3.7
	34	260.5	-

* FiA: fluid inclusions assemblage identified; † Fi: number of fluid inclusions measured in any single FiA.

TABLE DR4. EXPERIMENT DESIGN

layer	composition	density [g cm-3]	H [Wm-3]	initial thickness [m]	flow law
1	Upper Crust (sediments)	2600	1.52	2000	-
2	Middle Crust (schist, granite)	2650, 2700	1.2	36000	Bye, FV, quartzite
3	Lower Crust (felsic granulite 0.6; mafic granulite 0.4)	2900	0.42	32000	
4	Lithospheric Mantle (peridotite)	3500	0.035	130000	-

Bye = Byerlee's law, FV = Frictional-Viscous Flow Law (Bos & Spiers, 2002), Quartzite = Flow-Law of wet Quartzite (Gleason & Tullis, 1995)

Table DR5. EXPERIMENTS SET UP (SHEAR HEATING)

	timing of deformation			boundary conditions			RESULTS	
ID	start [Ma]	end [Ma]	Δt [Myrs]	ΔL [m]	dε/dt	notes	max T_{FZ} [°C]	$\Delta T_{FZ\text{-}WR}$ [°C]
0	-	-		-	-	background	195.7	0.0
1	38	24		10000	6.5E-14		236.7	41.0
2	38	24		15000	9.8E-14		247.9	52.2
3	38	24		20000	1.3E-13		258.2	62.5
4	38	24	14	25000	1.6E-13		268.7	73.0
5	38	24		30000	2.0E-13		279.4	83.7
9	38	24		50000	3.3E-13		282.0	86.3
10	38	24		5000	3.3E-14	variable strain-rate	227.7	32.0
10a	32	30		5000	2.3E-13		270.5	74.8
11	32	30		13000	5.9E-13		348.5	152.8
12	32	30	2	28000	1.3E-12		495.5	299.8
13	32	30		50000	2.3E-12		502.3	306.6
14	33	27		5000	2.3E-13		236.9	41.2
15	33	27	6	10000	4.6E-13		259.2	63.5

17	33	27		20000	9.1E-13		271.3	75.6
19	33	27		30000	1.4E-12		293.2	97.5
20	33	27		40000	1.8E-12		300.1	104.4
21	33	27		50000	2.3E-12		313.0	117.3
22	35	25		5000	3.8E-14		230.5	34.8
23	35	25		15000	4.6E-14		255.3	59.6
24	35	25	10	25000	5.7E-14		286.4	90.7
25	35	25		35000	7.6E-14		294.4	98.7
26	35	25		50000	1.1E-13		302.0	106.3
27	32	28	4	7000	2.3E-13		258.6	62.9
28	35	24	11	8500	6.5E-14		238.9	43.2
29	36	24	12	27000	7.8E-14		263.7	68.0
30	32	30	2	15000	9.7E-14		283.4	87.7
31	33	29	4	15000	1.3E-13		276.4	80.7
32	34	29	5	15000	1.9E-13		263.8	68.1
33	35	28	7	15000	3.9E-13		250.3	54.6
34	33	30	3	23000	1.8E-13		289.9	94.2
35	33	30	3	37000	2.1E-13		458.1	262.4
36	34.5	26	8.5	8000	2.6E-13		241.5	45.8

ID = experiment, Start = beginning of deformation [Ma], End = end time of deformation [Ma], Dt = duration of deformation [Myrs], □L = finite displacement accommodated by the fault [km], d□/dt = average strain-rate [s^{-1}], maxT_{FZ} = maximum temperature recorded within the fault core [°C], □T_{FZ-WR} = temperature difference between fault core and wall rocks [°C].

Table DR6 EXPERIMENTS SET UP (FLOW OF FLUIDS)

	timing of deformation			boundary conditions			RESULTS	
ID	**start [Ma]**	**end [Ma]**	**Δt [Myrs]**	**dϕ/dt**	**ϕ**	**notes**	**max T_{FZ} [°C]**	**ΔT_{FZ-WR} [°C]**
40	32	28	4	1.4E-13	0.10		196.3	0.6
44			4	2.8E-13	0.20		198.6	2.9

46			4	4.2E-13	0.30		199.7	4.0
48			4	5.7E-13	0.40		199.4	3.7
49			4	7.1E-13	0.50		217.3	21.6
50			4	8.6E-13	0.60		227.5	31.8
51	32		2	4.2E-13	0.15		203.6	7.9
52	31		1	8.50E-13	0.15		215.4	19.7
53	30.5		0.5	1.70E-12	0.15		235.7	40.0
54	30		0	8.50E-11	0.15	instantaneous flow	264.6	68.9
55	32		2	5.70E-13	0.2		216.3	20.6
56	31		1	1.10E-12	0.2		228.9	33.2
57	30.5		0.5	2.20E-12	0.2		243.4	47.7
58	30		0	1.10E-10	0.2	instantaneous flow	285.8	90.1
59	32.5		2.5	2.20E-13	0.1		217.6	21.9
60	31		1	5.70E-13	0.1		220.6	24.9
61	30.2	30	0.2	2.80E-12	0.1		248.2	52.5
62	33		3	1.10E-12	0.6		229.5	33.8
63	32		2	1.20E-12	0.6		236.0	40.3
64	30.5		0.5	6.80E-12	0.6		276.3	80.6
65	31		1	2.20E-12	0.4		242.4	46.7
66	31.5		1.5	1.90E-12	0.5		238.4	42.7
67	32.5		2.5	6.80E-13	0.3		222.0	26.3
68	30		0	3.40E-10	0.6	instantaneous flow	300.0	104.3
69	30		0	2.70E-10	0.5	instantaneous flow	300.0	104.3
70	33		3	4.10E-13	0.22		218.0	22.3
71	30		0	5.70E-11	0.1	instantaneous flow	255.0	59.3

ID = experiment, Start = beginning of fluid flow [Ma], End = end of fluid flow [Ma], □t = duration of fluid flow [Myrs], d□/dt = average flow rate of fluids [ms^{-1}], □ = finite volume of fluids to rock ratio [dimensionless], $maxT_{FZ}$ = maximum temperature recorded within the fault core [°C], $\square T_{FZ\text{-}WR}$ = temperature difference between fault core and wall rocks [°C].